The utilization of the double focal transformation for sparse data representation and data reconstruction

Kutscha, Hannes; Verschuur, Eric

DOI
10.1111/1365-2478.12362

Publication date
2016

Document Version
Accepted author manuscript

Published in
Geophysical Prospecting

Citation (APA)
Kutscha, H., & Verschuur, E. (2016). The utilization of the double focal transformation for sparse data representation and data reconstruction. *Geophysical Prospecting*, *64*(6), 1498-1515. https://doi.org/10.1111/1365-2478.12362

The utilisation of the double focal transformation for sparse data representation and data reconstruction

Dr. Hannes Kutscha *

EXPEC-ARC, Saudi Aramco; previously Department of Imaging Physics, Delft University of Technology

Dr. ir. D. J. (Eric) Verschuur †

Department of Imaging Physics, Delft University of Technology

*h.kutscha@tudelft.nl
†d.j.verschuur@tudelft.nl

Abstract

In many cases seismic measurements are coarsely sampled in at least one dimension. This leads to aliasing artefacts and, therefore, to problems in the subsequent processing steps. To avoid this, seismic data reconstruction can be applied in advance. The success and reliability of reconstruction methods is dependent on the assumptions they make on the data. In many cases wavefields are assumed to (locally) have a linear space-time behaviour. However, field data are usually complex, with strongly curved events. Therefore, in this paper we propose the double focal transformation as an efficient way for complex data reconstruction. Hereby, wavefield propagation is formulated as a transformation, where one-way propagation operators are used as its basis functions. These wavefield operators can be based on a macro velocity model, which allows our method to use prior information in order to make the data decomposition more effective. The basic principle of the double focal transformation is to focus seismic energy along source and receiver coordinates simultaneously. The seismic data is represented by a number of localized events in the focal domain, whereas aliasing noise spreads out. By imposing a sparse solution in the focal domain, aliasing noise is suppressed and data reconstruction beyond aliasing is achieved. To facilitate the process, only a few effective depth levels need to be included, preferably along the major boundaries in the data, from which the propagation operators can be calculated. Results on 2D and 3D synthetic data illustrate the method's virtues. Furthermore, seismic data reconstruction on a 2D field data set with gaps and aliased source spacing demonstrates the strength of the double focal transformation, especially for near-offset reflections with strong curvature and for diffractions.

Keywords: seismics, coarse sampling, reconstruction, inverse problem, sparse inversion, noise attenuation,

1 Introduction

In 3D seismic surveys the wavefields are sampled in four spatial dimensions, providing two lateral degrees of freedom (x and y) for both sources and receivers. The sampling is rarely dense in all four spatial dimensions. As a result, practical sampling geometries contain gaps and are coarse in one or more spatial dimensions. The reason for large data gaps can be faulty equipment, inaccessibility of certain areas or strong noise sources at certain locations such that the measured data become unusable. Also the near-offset range usually cannot be detected, because the sensitive detectors would be damaged if placed closely to a seismic source. The most common reason for coarse sampling, however, is the trade-off between geophysical and economical constraints. As coarse and incomplete sampling generates aliasing artefacts, for many applications the measured wavefield needs to be reconstructed to a dense and regular grid beforehand.

We suggest the double focal transformation for a seismic data reconstruction method that combines two features. First, it is transformation-based. Hence, the missing data in the data domain maps to aliasing noise in the model domain, where it can be suppressed ('de-noising'). Well-known other transformations that are used for seismic data reconstruction are the least-squares constrained Fourier transformation (Duijndam et al., 1999; Schonewille et al., 2009), the sparseness-constrained Fourier transformation (Xu et al., 2005; Zwartjes and Gisolf, 2006; Zwartjes and Sacchi, 2007; Zwartjes and Gisolf, 2007; Trad, 2009; Naghizadeh, 2012), the linear, parabolic and hyperbolic Radon transformation (Kabir and Verschuur, 1995; Herrmann et al., 2000; Trad, 2002; Trad et al., 2003; Wang et al., 2010; Verschuur et al., 2012) and the curvelet transformation (Hennenfent and Herrmann, 2008; Hennenfent et al., 2010; Naghizadeh and Sacchi, 2010). Often these methods are better suited to describe the data in the mid- and far-offset range. The near-offset range, on the other hand, is often very challenging due to the strong curvature of reflection events. Therefore, it cannot be described efficiently using these methods. This is especially true, if data-windowing cannot be applied successfully due to large data gaps.

Secondly, the double focal transformation is based on wavefield operators, which allow the utilisation of prior information of the subsurface for the reconstruction process. The main idea is that by utilizing subsurface information in combination with wavefield propagation a more redundant representation of the seismic data can be obtained. Examples of such approaches are wavefield continuation methods such as offset continuation (Bagaini and Spagnolini, 1996), shot continuation (Spagnolini and Opreni, 1996), DMO (Deregowski, 1986) and AMO (Biondi et al., 1998). All these methods have in common that they utilise the wavefield characteristics in a localised manner, where the involved operators are local convolution operators. Global solutions have been explored via least-squares migration, e.g. by Nemeth et al. (1999) and Kuehl (2002), where aliasing effects in the image could be suppressed, although the main objective there was not to reconstruct reliably new data. Trad (2003) extended the LS migration concept to data reconstruction, where he used the multi-offset image domain, under a sparseness constraint, to recreate seismic data. However, this process was not fully reversible yielding imperfections in the reconstruction.

The proposed double focal transformation describes the propagation in the subsurface with global wavefield operators. And it can do so in a reversible transformation manner, where forward (going from data space to model space) and inverse (going from model space to data space) double focal transformation represent inverse and forward propagation of the seismic data in both source and receiver coordinates. Please note that the focal reconstruction is - up to a certain extend - robust against inaccurate prior information, as we will demonstrate in this paper.

A predecessor of the proposed double focal transformation was presented by Berkhout and Verschuur (2006), which was called focal transformation, but it involved subsurface operators that described two-way seismic reflection events. The success of this reconstruction method was highly dependent in describing both propagation AND reflection in the subsurface. This puts a severe limitation to that method, as for complex subsurface models generating such operators (which basically resembled the major reflection events in the data) is a non-trivial task.

The newly defined double focal transformation only requires the description of rough propagation operators towards strategic depth levels, whereas the actual - difficult to obtain - reflection properties are estimated automatically by the method.

In this paper we demonstrate how the formulation of the double focal transformation can be obtained starting from the Rayleigh II integral. Similar to Kutscha and Verschuur (2012) we derive focal reconstruction as an inversion problem that is constrained by the sparseness promoting l_1 norm, which is utilised for aliasing noise suppression. Hereby, the velocity sensitivity of the chosen focal operators on the reconstruction result is analysed. In addition, we present a promising 2D marine field data (Gulf of Mexico) reconstruction result as well as the reconstruction of simple 3D synthetic data. Another novelty of this paper is the comparison of the 2D field data results with reconstruction results based on the sparse linear Radon transformation. Hereby, the benefits of these two methods for different parts of the data are demonstrated. Finally, we investigate how to improve the sparseness of the data representation by augmenting the double focal transformation with an additional linear Radon transformation.

2 Theory and implementation

2.1 The Rayleigh II integral in terms of convolution

The double focal transformation can be derived from the basic principles of wavefield extrapolation. To be more specific, it is based on the Rayleigh II integral, which allows the computation of a wavefield in a point from the measured wavefield along a flat plane (see Figure 1a). To compute the wavefield in point (x_A, y_A, z') the Rayleigh II integral for the three-dimensional space can be formulated in the frequency domain as:

$$P(x_A, y_A, z', \omega) = \iint_{-\infty}^{\infty} dxdy W^+(x, x_A, y, y_A, \Delta z, \omega) P(x, y, z_0, \omega), \tag{1}$$

with the wavefield propagation operator for a homogeneous medium between z_0 and z':

$$W^+(x, x_A, y, y_A, \Delta z, \omega) = \frac{1 + ik\Delta r}{(2\pi\Delta r)^2} \cos(\phi) e^{-ik\Delta r}. \tag{2}$$

Hereby, ω denotes the angular frequency and $k = \omega/c$ the wavenumber with c being the propagation velocity. Angle ϕ and distance Δr are explained in Figure 1a. Equation 1 describes wavefield propagation in terms of convolution with a wavefield operator along the x and y axes. This convolution integral extrapolates the wavefield from a plane in x, y direction at depth level z_0 to point A at depth z'. Please note that W^+ denotes downwards propagation (the plus for positive z direction).

In a similar way the 2D Rayleigh integral can be formulated as a convolution along the x-axis (see Figure 1b):

$$P(x_A, z', \omega) = \int_{-\infty}^{\infty} dx W^+(x, x_A, \Delta z, \omega) P(x, z_0, \omega), \tag{3}$$

with the 2D wavefield propagation operator for the homogeneous case:

$$W^+(x, x_A, \Delta z, \omega) = -\frac{ik}{2} \cos(\phi) H_1^{(2)}(k\rho). \tag{4}$$

Hereby, $H_1^{(2)}$ is the first order Hankel function of the second kind (see Abramowitz and Stegun, 1970). For an explanation of angle ϕ and distance ρ see Figure 1b. For more detailed information on the Rayleigh integral and its derivation from the Kirchhoff integral see e.g. Berkhout (1987) and Gisolf and Verschuur (2010).

Please note that in this paper only the explicit expression for W^+ in a homogeneous medium is described (equations 2 and 4). For the case of inhomogeneous velocity distributions the Rayleigh II integral can still be formulated as a convolution of a propagation operator with the data. In that case in equations 1 and 3 another propagation operator is used, where W^+ contains the impulse responses for the inhomogeneous layer between z_0 and z'. For more information see e.g. Berkhout (1982) and Gisolf and Verschuur (2010).

2.2 The WRW model

The data description used in the double focal transformation is based on the expression of wave-propagation by convolution integrals in the frequency domain (equations 1 and 3). Since this concept originates from the WRW model (Berkhout, 1982), we will give a short review of it here. For notation simplicity, we first consider the 2D case.

The discrete version of equation 3 is given as:

$$P(x_{k'}, z', \omega_n) = \sum_{k=1}^{K} \Delta x W^{+}(x_{k',k}, \Delta z, \omega_n) P(x_k, z_0, \omega_n). \tag{5}$$

This summation describes wavefield propagation from several discrete surface locations to one location in the subsurface. It can also be denoted as the multiplication of a row vector with a column vector. If we want to propagate to different lateral locations $x_{k'}$ in the subsurface z' we get a system of equations that also can be denoted as a matrix-vector multiplication. In our area of interest $P(x_k, z, \omega_n)$ is used as a source wavefield e.g. at the surface z_0. Therefore, we change the notation from P to S. Furthermore, in seismic data acquisition usually many source experiments are acquired. Therefore, we have many column vectors, which are combined in the source matrix $\mathbf{S}(z_0)$. Hence, matrix equation $\mathbf{P}(z') = \mathbf{W}^{+}(z', z_0)\mathbf{S}(z_0)$ describes the downward propagation of many source experiments to many subsurface points along depth level z'. Reflection events of a complete seismic acquisition in 2D can be described in this matrix notation by the following equation:

$$\mathbf{P}(z_0) = \mathbf{D}(z_0) \sum_{m=1}^{M} \left[\mathbf{W}^{-}(z_0, z_m)\mathbf{R}(z_m)\mathbf{W}^{+}(z_m, z_0)\right] \mathbf{S}(z_0). \tag{6}$$

Note that by conventionally multiplying these matrices from the right to the left causality of wavefield propagation is obeyed intrinsically: The source matrix $\mathbf{S}(z_0)$ represents all downgoing source wavefields at the surface, with every column containing the wavefield for one seismic experiment. This is then downward-continued by propagation matrices $\mathbf{W}^{+}(z_m, z_0)$ to M levels with the corresponding depths $z_m = m\ \Delta z$. Hereby, the step-size in z direction (Δz) needs to be small enough (e.g. 5 meter) for a detailed representation of physical reflection responses. Every element of such a propagation matrix $\mathbf{W}^{+}(z_m, z_0)$ describes the propagation of a wavefield in point (x_k, z_0) to a point in the subsurface $(x_{k'}, z_m)$. If the downward propagated wavefield reaches a reflecting boundary at depth z_m, two mechanism enter the propagation model: reflection and transmission. The reflectivity matrix $\mathbf{R}(z_m)$ turns the downward propagating wavefield $\mathbf{P}^{+}(z_m) = \mathbf{W}^{+}(z_m, z_0)\mathbf{S}(z_0)$ into an upward propagating wavefield $\mathbf{P}^{-}(z_m) = \mathbf{R}(z_m)\mathbf{P}^{+}(z_m)$. Every row vector of $\mathbf{R}(z_m)$ contains a convolution operator that applies the angle-dependent reflection to the incident wavefield related to one spatial location. For more information about the reflectivity matrix see Berkhout (1987), de Bruin et al. (1990), Doulgeris et al. (2009) and Kutscha (2014). The reflected wavefield is then upward propagated to the receivers at the surface. The propagation from any depth level z_m to z_0 is described by $\mathbf{W}^{-}(z_0, z_m)$ in equation 6, where the '-' superscript denotes negative z direction. The process of data creation with the WRW model (equation 6) is visualised in Figure 2a.

2.3 Extension to three dimensions

Wavefield extrapolation in 3D can be discretised similarly to the 2D case. For a better understanding let's denote the discrete version of the 3D integral (equation 1):

$$P(x_{k'}, y_{l'}, z', \omega_n) = \sum_{l=1}^{L} \sum_{k=1}^{K} W^{+}(x_{k',k}, y_{l',l}, \Delta z, \omega_n) P(x_k, y_l, z, \omega_n) \Delta x \Delta y. \tag{7}$$

It describes the propagation of the wavefield at all discrete points along the 2D plane at z_0 to the grid-point at $(x_{k'}, y_{l'}, z')$ for one temporal frequency. This double summation can be formulated also as a vector-vector multiplication. Hereby, very long vectors are formed that are concatenations of vectors with constant y coordinate (see Kinneging et al., 1989). Like in 2D the propagation of the wavefield at the surface to many points in the subsurface and the usage of several sources at the surface will turn this vector multiplication into matrix multiplication $\mathbf{P}(z') = \mathbf{W}^{+}(z', z_0)\mathbf{S}(z_0)$. As a result, the description of reflection events in 3D can be denoted in the same way as in 2D with equation 6. Note that 3D leads to a block-structure of all matrices in equation 6 as they consist of sub-matrices with constant y. For more information see Berkhout (2006).

In both 2D and 3D different rows of the data matrix $\mathbf{P}(z_0)$ correspond to different receiver gathers, while different columns represent different shot records (source gathers). Any diagonal of the data matrix corresponds to a monochromatic common-offset gather. Due to reciprocity the data matrix is symmetric along the zero-offset (main-) diagonal.

2.4 From the WRW model to the concept of double focal transformation

In contrast to the WRW model, the double focal transformation estimates the reflectivity only for a limited number of N depth levels. Note that for the sake of simplicity we assume a fixed spread acquisition design, where a source is fired at each receiver location for consecutive source experiments. Data creation with the model of double focal transformation is formulated as:

$$\mathbf{P}(z_0) = \hat{\mathbf{D}}(z_0) \sum_{n=1}^{N} [\hat{\mathbf{W}}^{-}(z_0, z_n) \mathbf{X}(z_n) \hat{\mathbf{W}}^{+}(z_n, z_0)] \hat{\mathbf{S}}(z_0), \tag{8}$$

which is visualised in Figure 2b. Compared to equation 6, the hatted symbols now indicate that only approximate operators are used, i.e. based on an approximated velocity model. Furthermore, instead of using M depth levels with a distance of Δz, only a subset of N depth levels is used, usually distributed over the whole depth range. The N depth levels can be chosen strategically in order to coincide with prominent reflectors in the data ($N << M$). Please note, since for each depth level *two* focal operators are used, one propagating energy from the source locations at the surface to the subsurface and one propagating energy from the subsurface to the detector locations at the surface, there will be essentially two focusing steps later on. This explains the name *double* focal transformation.

The consequence of using fewer depth levels and approximate propagation operators $\hat{\mathbf{W}}^{+}(z_n, z_0)$ is that seismic energy will not necessarily be focused at offset and time zero in the reflectivity matrices $\mathbf{R}(z_m)$, which was assumed to be the case in the WRW model. Therefore, the reflectivity matrices have been replaced by focal domains $\mathbf{X}(z_n)$, representing frequency slices of a fully sampled, inverse or backward propagated data set.

Please note, that in practice we don't know the source properties (source wavelet, source directivity, source to source variation) precisely. The same is true for the receivers properties. For our experiments, therefore, $\hat{\mathbf{D}}$ and $\hat{\mathbf{S}}$ are redundant and can be omitted in equation 8. This leads to:

$$\mathbf{P}(z_0) = \sum_{n=1}^{N} [\hat{\mathbf{W}}^{-}(z_0, z_n)\mathbf{X}(z_n)\hat{\mathbf{W}}^{+}(z_n, z_0)]. \tag{9}$$

In this equation source and receiver properties are absorbed by the focal domain $\mathbf{X}$. In general the focal domain absorbs everything that is not fully explained by the data model, for instance transmission effects. Note that for other experiments, which e.g. include source and receiver arrays or blended acquisitions, it is still essential to formulate the source matrix and receiver matrix explicitly.

As shown in Figure 2b we only use the strongest contrasts in the subsurface to determine the depth of the levels from which we generate the focal operators. Because, reconstruction is a pre-processing step, at that stage a very good velocity model might not be available. Therefore, we demonstrate the effect of an accurate and an inaccurate focal operator on a simple dataset containing only three reflection events. In many cases we know the velocity of the uppermost layer. In a marine situation this would just be the water velocity. Therefore, the first focal operator is generated based on an accurate velocity model. However, for the generation of the second focal operator we choose a depth level, which is between the depth levels of the actual second and third reflector. Also, the second focal operator is based on an approximate velocity being a representative NMO velocity. The matrices of equation 9 corresponding to this case are denoted in Figure 3.

In Figure 3 it is shown that the data representation in the focal domain is very sparse. For any frequency the data matrix $\mathbf{P}(z_0)$ is almost completely filled with energy, while the energy of the first reflector is represented by just a line in the first monochromatic focal domain $\mathbf{X}(z_1)$, and energy of the second and third reflector is located around the main diagonal in the second monochromatic focal domain $\mathbf{X}(z_2)$.

Inverse Fourier transforming equation 9 changes the matrix multiplications in the frequency domain to multi-shift convolutions (an operation closely related to a 2D convolution) in the time domain. The time representation of Figure 3 is shown in Figure 4. As we can see, here, the data compression of the first reflection event is even more efficient.

The complete 3D data cube $\mathbf{p}(z_0)$ containing the first hyperbolic reflection event is represented by a band-limited line (marked in red). This line forms a diagonal around time zero in the first focal domain $\mathbf{x}(z_1)$. This additional compression is the reason why the time-implementation of the double focal transformation is chosen for data reconstruction. The second and third reflection event are not completely focussed and have residual spatial phase. The assumed depth of the second focal operator is in between the depths of the actual second and third reflector. Therefore, the second reflection event is over-corrected (curved upwards and above zero time) and the third reflection event is under-corrected (curved downwards and below zero time) in the second focal domain $\mathbf{x}(z_2)$. Still these events are compressed compared to the input data. For a better understanding the middle shot record and the middle sections of the first and second focal domain are shown in Figure 5.

2.5 Comparison to Born modelling

It is important to notice that the data model of the double focal transformation is fundamentally different form other methods like Born modelling. Instead of using every possible depth level (e.g. every 5 m) we use a few representative levels, which can differ hundreds of meter in depth. Also, instead of using (complex-valued) scalars to describe reflection coefficients in the frequency domain at certain subsurface points, we use whole data volumes (focal domains), which describe an extended reflectivity in the time domain. These focal domains have a spatial dimension to describe angle dependency and they have a temporal dimension large enough to cover all reflections within a certain depth area.

3 The double focal transformation as an inverse problem

As mentioned in the introduction we present a method that formulates the physical process of wave propagation as a transformation such that state-of-the-art aliasing noise suppression methods can be applied in the transform domain. This can be achieved by bringing equation 9 to the form of:

$$\vec{p} = \mathbf{L}\vec{x}. \tag{10}$$

Hereby, $\vec{p}$ is the data in the time domain denoted as a long vector (all columns of the 3D cube concatenated) and $\vec{x}$ consists of vectorized focal domains all connected to a long vector. The operator $\mathbf{L}$ can be formulated in principle as an explicit matrix. However, since it would represent a huge convolution matrix, this is not done in practice. Therefore, $\mathbf{L}$ is formulated as a function that contains the following steps:

1. Resort the focal domains from a long vector $\vec{x}$ to 3D tensors $\mathbf{x}(z_{1\ldots N})$.

2. Transform these tensors from the time domain to the frequency domain.

3. Multiply every frequency slice of each focal domain with the frequency slices of the corresponding focal operator, to derive the data matrix (Equation 9). This is displayed by Figure 3.

4. Transform the derived data from the frequency domain to the time domain to obtain the 3D data tensor $\mathbf{p}$.

5. Finally, vectorising data tensor $\mathbf{p}$ yields $\vec{p}$.

Many transformation-based reconstruction methods invert such an equation in a stabilised way to obtain an aliasing-free model space from coarse input data. Examples are the Fourier transformation (Zwartjes and Sacchi, 2007), the Radon transformation (Kabir and Verschuur, 1995) or the curvelet transformation (Hennenfent et al., 2010).

3.1 Forward double focal transformation

Until now we have just demonstrated that data creation with the model of double focal transformation can be formulated as a matrix vector equation. In the form of equation 10 this is called the *inverse double focal transformation*, because it transforms from the model space to the data space. This is in most cases a well-posed problem and easy to compute. However, our aim is to derive the focal domain from the, eventually coarse, input data. This process is called *forward double focal transformation*. It has to be realised that the transformation matrix $\mathbf{L}$ is not orthogonal by nature and, thus, can not be inverted. Still, there are several possibilities to estimate $\vec{x}$. For instance equation 10 could be multiplied with $\mathbf{L}^H$ which is the conjugate-transpose of $\mathbf{L}$. This would lead to a rough estimate of $\vec{x}$. Another possibility is to solve for $\vec{x}$ by least-squares inversion or by sparse inversion, which is also investigated in Kutscha and Verschuur (2012) and Kutscha (2014). This paper will focus solely on the case of sparse inversion as this shows the best reconstruction results for coarse input data.

The forward double focal transformation by sparse inversion can be formulated as the so-called "Basis Pursuit De-noise" problem (van den Berg and Friedlander, 2008):

$$\underset{\vec{x}}{\text{minimise}} \; ||\vec{x}||_1 \text{ subject to } ||\vec{p} - \mathbf{L}\vec{x}||_2 \leq \sigma. \tag{11}$$

In equation 11 the l_1 norm of the focal domain is minimised while keeping the l_2 norm of the data misfit smaller than the scalar σ, which is most commonly the noise level of the input data. Hence, a focal domain with the minimum absolute value is searched that still provides an acceptably small data misfit at the known traces. All results in this article using the l_1 constraint are computed with the spgl1 solver (van den Berg and Friedlander, 2008), where spgl1 stands for Spectral Projected Gradient - l_1.

For a more realistic scenario random noise has been added to the input data that was used in Figures 3 to 5. Hereby, in Figure 6a and b least-squares inversion was used and in Figure 6c and d sparse inversion was used. The least-squares

constraint tries to smear the model parameters as much as possible by rather using many weak parameters than using a few strong ones. Therefore, in Figure 6a and b the three reflectors are mapped to the first focal domain as well as to the second focal domain ("model space leakage") explaining every event twice. Also, the first reflector is not mapped to a band-limited spike in the first focal domain, as we would expect, but to a so-called correlation cross, which explains first reflector in the input data as good as a band-limited spike would do. Furthermore, correlation artefacts are visible in this result. The sparseness constraint, on the other hand (the term $||\vec{x}||_1$ in equation 11) aims to use as few model parameters as possible, hence, preferring a few strong parameters over many weak ones. In Figure 6c and d the sparseness constraint forced the solution space to have as few non-zero elements as possible, which automatically suppresses the correlation artefacts and the model space leakage. Obviously, the forward double focal transformation is a non-unique process and solutions depend on the chosen model constraint. Both, the least-squares and the sparse solution have a very similar data-misfit, so just from this observation neither one is preferred. However, as we will see in the next section, the aliasing noise that is generated by coarse input data is smeared out over a certain area in the focal domain. It can be, hence, better suppressed by a sparseness constraint than by a least-squares constraint.

3.2 Coarse input data

In the previous examples it was assumed that the input data is dense. In the case of missing traces $\vec{p}$ becomes shorter. It is important to notice that the model vector (focal domain) is always defined on the dense grid and so it keeps the same size. As a result, equation 10 becomes more under-determined.

To show the effect of missing traces in our example, three out of four traces have been removed from the dense input data. Again, the focal domain has been estimated by least-squares inversion for the purpose of demonstration. In Figure 6e and f it can be observed that the least-squares constraint by itself does not suppress aliasing noise, but leaves it in the model space. The missing traces in the data lead to a stripe-pattern (edged by red shapes). The aliasing noise is clearly separated from the data content.

In Kutscha (2014) it is shown how de-aliasing filters can be generated for simple data that are coarsely sampled in a regular fashion. These filters can be used to mute the noise area in the focal domain, for instance by setting to zero the energy in the red shapes in Figures 6e and f. A similar approach was already proposed by Berkhout et al. (2004). Another option is to use a weighting function for the model space, which allows a more flexible suppression of aliasing noise (see Kutscha, 2014). However, a more robust way is to estimate the focal domain from the coarse input data by sparse inversion. This allows also to handle complex data and irregular undersampling without assumptions on the local distribution of the aliasing noise. The reason why a sparseness constraint to the focal domain can successfully suppress aliasing noise is because the data content is focused in the focal domain (sparse data representation) while aliasing noise spreads out (is not sparsely represented).

For the case of coarse input data, equation 11 can be used again except that we only compare the data misfit at the measured traces:

$$\underset{\vec{x}}{\text{minimise}} \; ||\vec{x}||_1 \text{ subject to } ||\vec{p} - S\{\mathbf{L}\vec{x}\}||_2 \leq \sigma, \tag{12}$$

where $\vec{p}$ now is coarsely sampled and the sampling operator S only picks the traces corresponding to the available measurements from the estimated data. Hence, in equation 12 less traces are available for the computation of the data misfit which makes the inversion problem more ill-conditioned. Therefore, the objective function becomes even more dependent on the sparseness constraint, which now not only enables a sparse data representation but also enables the suppression of aliasing noise in the focal domain.

As a result each focal domain in Figures 6g and h shows the data content but not the aliasing noise and, hence, represents a focal domain that corresponds to the dense input data (compare to Figures 6c and d). Note that the process of obtaining $\vec{x}$ resembles the difficult reconstruction step. Transforming this focal domain back to the data space for any desired output sampling (equation 10) is then again a trivial process.

In Figures 6e and f we showed that aliasing noise is relatively well separated in the focal domain. This is not the case when investigating the coarse input data in the FK domain as is shown in Figure 7a. Within the red circles, signal content and aliasing noise overlap and would be difficult to separate in this domain. On the other hand in Figure 7b you can clearly see that using focal reconstruction not only removed the aliasing noise, but also preserved all the signal content.

3.3 The influence of imprecise focal operators

In Figure 6c-d we see that we can focus the first reflection event to a band-limited spike, because the corresponding focal operator is based on an accurate velocity distribution. However, reflection events two and three were not represented so sparsely, because the second focal operator was based on an imprecise velocity distribution which leads to an incomplete focussing.

In general, the double focal transformation is almost not influenced by structural and velocity errors of the macro model on which the focal operators are based, if these errors are within a certain range. Since the same focal operators (eventually imprecise) are used to derive the focal domain (e.g. by equation 11) and to transform back to the data space (equation 10) the data is always matched at the original traces. However, the sparseness of the data representation in the focal domain influences the reconstruction quality.

In Figure 8 a quantitative evaluation of the previous statement is depicted. Here a plot of the reconstruction error

for dense and coarse data as a function of velocity error in the focal operator is displayed for a dataset with one reflection event. In the case of dense input data (Figure 8a) the following can be observed: If the focal operator is based on a velocity model with too low velocities, the reconstruction is almost not influenced, even by velocity errors up to -500m/s. The focal domain then contains residual phase, which is corrected for by applying the erroneous focal operator also for the inverse double focal transformation. If the focal operator is based on too high velocities, on the other hand, the data mismatch increases more prominently. Also in this case the events are not completely focused in the focal domain, which, like mentioned before, should be corrected for by the inverse double focal transformation. However, a focal operator with a too high velocity acts as a velocity filter on the data. The larger the velocity error, the more the data is harmed. The focal operator automatically filters all energy outside its spatial bandwidth meaning that high angles are lost. It is, hence, suggested to always prefer focal operators based on slightly too low velocities rather than focal operators based on slightly too high velocities.

For real, coarsely sampled input data there is no possibility to evaluate the reconstruction in the data gaps objectively. Therefore, only the measured traces are taken into account for the computation of the data-misfit. In that case the data-misfit dependency of the velocity-error of the focal operator is very similar to the case of dense input data (Figure 8a). For synthetic data, on the other hand, the dense input data is actually available for comparison. In Figure 8b the reconstructed data is compared at all traces, even though the utilised input data was coarse. The same is of course possible if densely sampled field data is available, which can be undersampled afterwards to test the reconstruction algorithm. It can be observed that the data mismatch increases almost equally for both, focal operators based on too high velocities and based on too low velocities. Since in both cases the data isn't properly focused, the assumption that the data is sparsely represented in the focal domain is not fully correct any more. That decreases the capability to distinguish the weak dispersed aliasing noise from strong focused signal energy in the focal domain, and, therefore, decreases the reconstruction quality. For the current example a velocity error of roughly $-200m/s$ to $+200m/s$ is tolerable for decent reconstruction results. This range is, of course, data-dependent.

Note that the robustness of this method against inaccuracies in the focal operators is not only utilised for seismic data reconstruction (Kutscha et al., 2010), but also for primary estimation (Lopez and Verschuur, 2013) and deblending (Doulgeris et al., 2012; Kontakis and Verschuur, 2014).

4 Results

4.1 2D Field data

In the following the double focal transformation is utilised for the reconstruction of a 2D marine data set from the Gulf of Mexico (Mississippi Canyon, see Dragoset, 1999) that was provided by WesternGeco. The double focal transformation is principally defined for all geometries and sampling scenarios. However, currently it is implemented for

fixed-spread geometries based on a regular sub-grid only. Therefore, the marine moving-spread acquisition geometry is translated to a fixed-spread acquisition geometry using reciprocity (Fokkema and van den Berg, 1993), which changes the (moving-spread) near-offset extrapolation problem to a (fixed-spread) gap reconstruction problem.

The fixed-spread acquisition that is derived in that way for this example consists of 101 source gathers with each 101 receivers. It is sampled in the time domain with $\Delta t = 6ms$ and the original source and receiver sampling is $\Delta x_{rcv} = \Delta x_{src} = 26.67m$. The maximum frequency is $60Hz$. To further challenge our proposed reconstruction algorithm, a sampling operator is applied to the input data, deleting two out of three measured sources. Thus, the new source spacing Δx_{src} is roughly $80m$ and the near offset gap is $213.4m$.

In Figure 9a a typical receiver gather of the full, coarse data set is displayed, where empty traces were put at the missing locations. Note that the amplitude in the data plots has been clipped to 20 percent of the maximum of the input data for a better visibility of the weak events.

As you can clearly see in Figure 10a, real data usually contain a large number of reflections. Choosing a focal operator for each reflector would be very computationally expensive and, hence, inefficient and infeasible. Usually, a strategic choice is made in order to accomplish the best trade-off between sparse data representation and computational cost. In our case four depth levels are used ($N = 4$). From each level a focal operator is generated based on the corresponding NMO velocity. As done in Berkhout and Verschuur (2006), the choice of these levels depends on the strongest reflection events in the data. However, the depth levels only have to be roughly in the range of strong reflectors and don't need to follow the varying depths exactly (see Kutscha and Verschuur, 2012; Kutscha, 2014).

However, with these four focal operators the coarsely sampled data is transformed into four sparse, densely sampled focal domains by 200 spgl1 iterations solving equation 12. The middle sections of these four focal domains are displayed in Figure 10. In our example the chosen focal operators focus one or more reflections of a certain depth area of the data around zero time in its corresponding focal domain, which can be observed in Figures 10(a-c). We also can see some leakage of energy in between the different focal domains. Especially, the fourth focal domain (Figure 10d) in its upper part contains energy from shallower reflections that are also partly mapped in the other focal domains. By itself this is not a problem as all focal domains together explain the input data. The fact that the fourth focal domain is not that sparse can be explained by the trade-off between data misfit and sparseness in the focal domain. For a high number of spgl1 iterations more and more weak details in the estimated data are used to decrease the data misfit. These details can often not be represented in a sparse way. However, the data representation is still sparse enough to enable the aliasing noise suppression efficiently.

Next, the focal domains are simply transformed to the dense data grid ($\Delta x_{rcv} = \Delta x_{src} = 26.67m$) with the inverse

double focal transformation (equation 10). Figure 9b shows a very good reconstruction result, where the regularly undersampled data is reconstructed properly (worst case scenario for Fourier-based methods) as well as the near-offset gap. Note that strong events are reconstructed as well as weak events and diffractions are handled properly, too.

In order to evaluate the capabilities of the double focal transformation for data reconstruction, it is compared to a state-of-the-art, sparse, linear Radon reconstruction method, as described by Trad et al. (2003) and Verschuur et al. (2012). To make use of the redundancy of the data five receiver gathers were reconstructed simultaneously with the 3D sparse linear Radon transformation (receiver, source, time). In Figure 9d and 9f the reconstruction results of this method for the near and mid/far offset range are compared to the result of the double focal transformation in Figure 9c and 9e. As is clearly visible in Figure 9d the near-offset gap is not reconstructed satisfactorily because strongly curved events are not efficiently represented in the linear Radon domain. This leads to a poorer reconstruction of the curved, strong reflector at around 2.4 seconds in the linear Radon result in Figure 9d compared to the focal reconstruction result in Figure 9c. Also diffractions are hardly visible in the Radon result whereas they are properly reconstructed when using the double focal transformation. However, for the mid/far offset range of this dataset, where events are mostly (locally) linear and they can be represented efficiently in the linear Radon domain. Actually, the reconstruction result of the linear Radon transformation looks sharper and more consistent in the mid/far offset range in Figure 9f than the focal reconstruction result in Figure 9e, in which at least the first reflector is still slightly aliased.

It has to be mentioned that there are alternative ways to make use of the linear Radon domain for seismic data reconstruction. For instance it can be applied to NMO corrected CMP gathers (as was also done in Verschuur et al., 2012) or to COVTs (Common Offset Vector Tiles, see Cary, 1999), where the seismic events are generally represented more linearly than in receiver gathers (except again for diffractions). However, to fully exploit such domains the earth is assumed to be laterally smooth, whereas the focal domain is aiming at reconstructing data from more heterogeneous structures. For a comparison of our method with seismic data reconstruction based on the parabolic Radon transformation, see Kutscha (2014).

4.2 3D synthetic data

When reconstructing in three dimensional space (x,y,z), the resulting data have five coordinates (receiver-x; receiver-y; source-x; source-y; and time). Thus, reconstruction for such a data volume is usually referred to as '5D reconstruction' (Trad, 2009). Conveniently, the formulation of the forward and inverse double focal transformation stays exactly the same (equation 11 and 10). However, data vector $\vec{p}$ and model vector $\vec{x}$ now contain 3D instead of 2D data, hence, the whole 3D dataset (within the considered aperture) is reconstructed at once. For more information on the 3D implementation, see Kutscha (2014). The formulation of the implicit function $\mathbf{L}$ in 3D is equivalent to the one in 2D.

Note that the data compression in 3D is by one order more efficient than in 2D (see Kutscha, 2014) which allows a

sparser data representation and, thus, a better data reconstruction. Furthermore, the 3D implementation can make use of the redundancy in the data in both lateral directions, which increases the reconstruction capability.

Initial results for the 3D focal reconstruction are obtained for simple, synthetic data from a small one-reflector medium in order to prove the concept (Figure 11). Note that the dense input data was decimated in a way that only 7% of the traces remained (Figure 11a). After 3D-double-focal transformation all traces are reconstructed (Figure 11b). Reconstruction tests for real data or larger, complex synthetic data are not yet possible because of the large memory requirements of the current implementation.

5 Sparser data representation via cascaded linear Radon transform

As demonstrated, the double focal transformation is a very efficient sparse data representation for reflection data. However, in some reconstruction cases even sparser solutions are desired e.g. to suppress the aliasing noise stronger or avoid leakage of energy between the focal domains using the multi-level implementation. One solution is to change the l_1 norm to a sparser norm (e.g. l_0 or Cauchy). However, doing this we would loose the desired stability of the l_1 solution. Therefore, our favoured approach is to keep the l_1 norm and just make the data representation itself sparser.

To further increase the sparseness of the data representation, an additional linear Radon transform in both spatial directions of the focal domain can be applied. Hereby, the similarity of the data along the diagonal in the focal domain is utilised for additional data compression. Note that this will be the case if the earth is (locally) laterally smooth in one spatial direction. In order to use this concept for data reconstruction a problem like equation 12 is solved. The difference is that $\mathbf{L}$ represents the inverse double focal transformation and the inverse Radon transformation combined to one transformation.

The process of data reconstruction using this combined transformation is illustrated on a 2D synthetic dataset, which consists of a fixed spread acquisition corresponding to a model with one plane and one dipping reflector. In Figure 12a the corresponding focal domain is displayed for the case that the perfect focal operator for the first reflector is used. This display is done in a 3D fashion by making all data samples with values below a certain threshold invisible. As expected, the first reflector is focused to a diagonal event through the focal domain similar to the first focal domain in Figure 4. The second reflector is not completely focused and has residual spatial phase. Applying a linear Radon transformation in both lateral directions of the focal domain the double-radon-focal domain $\theta(z')$ is generated as displayed in Figure 12b. As can be observed, no compression for the first event in the focal domain was accomplished, because it was transformed from a linear event into another linear event. But the energy corresponding to the second reflector, which consisted of a set of hyperbolic events in the focal domain, could be transformed around a single band-limited elliptic locus.

Note that utilising the linear Radon transformation also has the capability to compress the 'crosses' in the focal domain that are generated by the AVP differences between the data and the focal operators (see Berkhout, 1997; van Wijngaarden, 1998).

In Figure 13 coarse input data is reconstructed using in one case the double focal transformation and in the other case double-focal-double-radon transformation. For both cases 10 spgl1 iterations were used. It is clearly visible that in the first case the first reflector is properly reconstructed but the second one, for which no focal operator was available, is less well reconstructed. Since the first reflector can be represented much sparser in the focal domain than the second one, it is picked up much earlier by the spgl1 solver. More spgl1 iterations would be needed to add enough parameters to the model space in order to fully explain the second reflector. On the other hand, in the second case with the double-radon-double-focal transformation both reflectors are reconstructed equally well. The extra linear Radon transformation improves sparseness of the data representation, which allows a sufficient reconstruction with less model parameters. The improved reconstruction for reflection events which are not completely focused by the focal operator provides the opportunity to use less depth levels in the multi-level implementation of the double focal transformation (smaller N in equation 9) in combination with a double-radon transformation.

However, some artefacts were introduced as well in Figure 13c. This is the result of an undersampling in the linear Radon domain, which means that the step-size Δp needs to be decreased in order to satisfy the sampling criterion.

6 Discussion and outlook

We demonstrated that having an adequate focal operator is important for the complete focusing of a reflection event into a band-limited spike. Assuming then that in a real data case for *every* true reflector the *perfect* focal operator would be available, the data could be represented by band-limited spikes in their corresponding focal domains, which allows data reconstruction for very large data gaps. As mentioned before, with the current implementation memory usage and computational cost are increased drastically when the number of focal operators is increased. This would make such an attempt infeasible. However, if the double focal transformation would be implemented in a way that only a few parameters in the centre of each focal domain are considered, this problem might be avoided. Actually, if only the central parameters of the focal domains are considered, assuming a perfect velocity model, the double focal transformation actually represents a sparse, least-squares migration algorithm.

By comparing the strengths and weaknesses of the double focal transformation with the linear Radon transformation (Figure 9) for different parts of the data it becomes obvious that a combination of both methods into a hybrid one

might be a very interesting field of study. A first implementation for the purpose of deblending has been reported by Kontakis and Verschuur (2015).

As mentioned before, one critical aspect of the double focal transformation are the computational costs. Applying the forward double focal transformation basically means to invert for $\mathbf{L}$ in equation 10. This is done by applying $\mathbf{L}$ and $\mathbf{L}^H$ many times in order to minimise an objective function like equation 11 by e.g. the spgl1 solver. Therefore, we investigate the cost of applying operator $\mathbf{L}$ to the focal domain $\vec{x}$. The five basic steps of this operator application were described before, whereby only the matrix multiplications (step 3) are computationally expensive and, hence, determine the computational speed of the focal reconstruction. Each matrix has the size of number of sources by number of receivers. By up-scaling the problem-size the cost of performing these matrix multiplications increases super-linearly. When for instance considering realistic 3D acquisition geometries these matrices can quickly become very large.In order to provide some numbers: The marine field data example was reconstructed using 200 spgl1 iterations on a typical desktop computer (Intel®Xeon®Processor $E3-1240\ v2$) in less than an hour. The memory load per data cube (data, focal domain, focal operator) is ca. 20MB.

In order to decrease the memory requirements and computational costs in future implementations only a couple of elements in the focal domains around their focal points could be considered. This would of course require that the seismic events are sufficiently focussed around the focal points in order to avoid the loss of signal content. Furthermore, in the current implementation the focal operators (in the frequency domain) are pre-computed and loaded into memory and then simply are applied like in equation 9. Another option would be to generate the focal operators "on the fly". This would reduce the memory requirements but instead increase the computational costs instead.

7 Conclusions

It has been demonstrated that the double focal transformation allows a physical and very efficient parametrisation of seismic reflection and diffraction data. The sparseness of the data-representation in the focal domain and its robustness against the usage of inaccurate focal operators allows a very satisfying reconstruction of complex data that are regularly undersampled and contain large gaps. The method was demonstrated for 2D and 3D synthetic data and 2D field data. Furthermore, the proposed method was evaluated based on the 2D field data set by comparing its performance with the linear Radon reconstruction, where the focal reconstruction was clearly better for the chosen data at small to medium offsets.

To further compress the seismic signals, the double focal transformation was augmented with the linear Radon transformation. The potential benefits of combining these two transformations could clearly be demonstrated.

8 Acknowledgements

We would like to thank Professor Berkhout and the sponsors of the Delphi consortium for their support. WesternGeco is acknowledged for providing the seismic field dataset and we greatly appreciate Laurens Krügers contribution to the results of Figures 12 and 13.

List of Figures

9 Figures

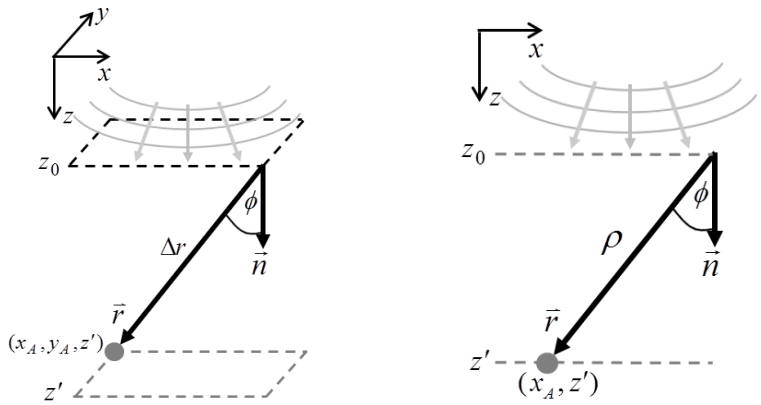

Fig. 1: In (a) the schematic illustration of the downward propagation of the wavefield from any point at the surface (x, y, z_0) to a certain point in the subsurface (x_A, y_A, z') is shown in 3D. Hereby, $\vec{\mathbf{r}}$ is the vector connecting these two points, $\vec{\mathbf{n}}$ the downward pointing normal vector of the surface and ϕ the angle in between them with $\cos(\phi) = \Delta z/\Delta r$. In (b) the 2D case is displayed. Hereby, ρ represents the distance between any surface point (x, z_0) and subsurface point (x_A, z') and $\cos(\phi) = \Delta z/\rho$.

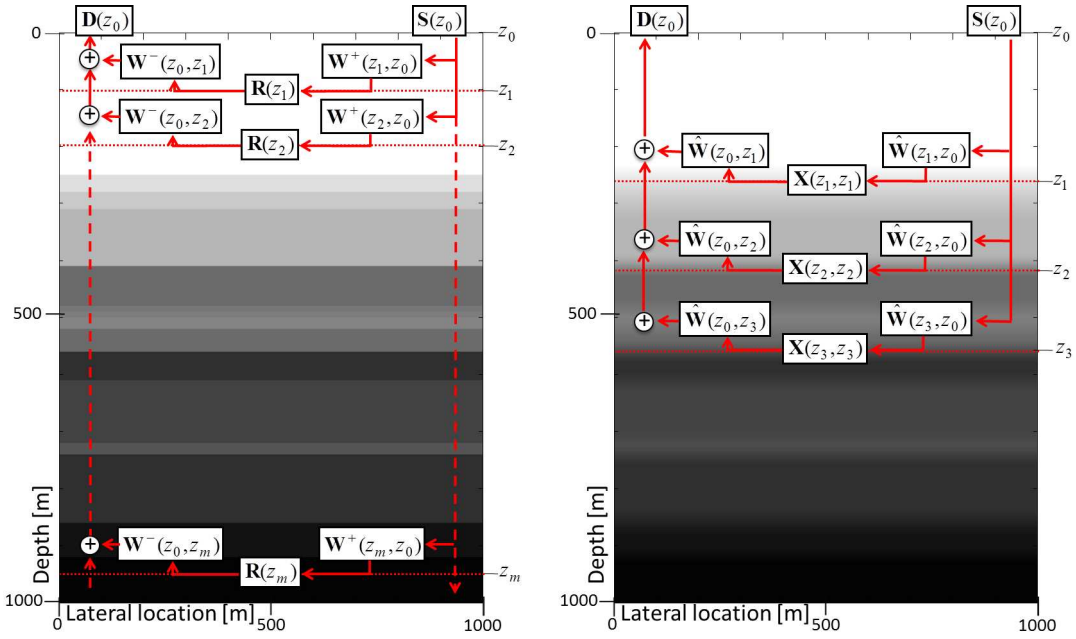

(a) (b)

Fig. 2: Concept for seismic data description using (a) the WRW model and (b) the double focal transformation. For the WRW model every depth level (e.g. every $5m$) is considered, regardless of the actual subsurface structure. For the double focal transformation, on the other hand, only depth levels are considered where prominent reflectors are expected.

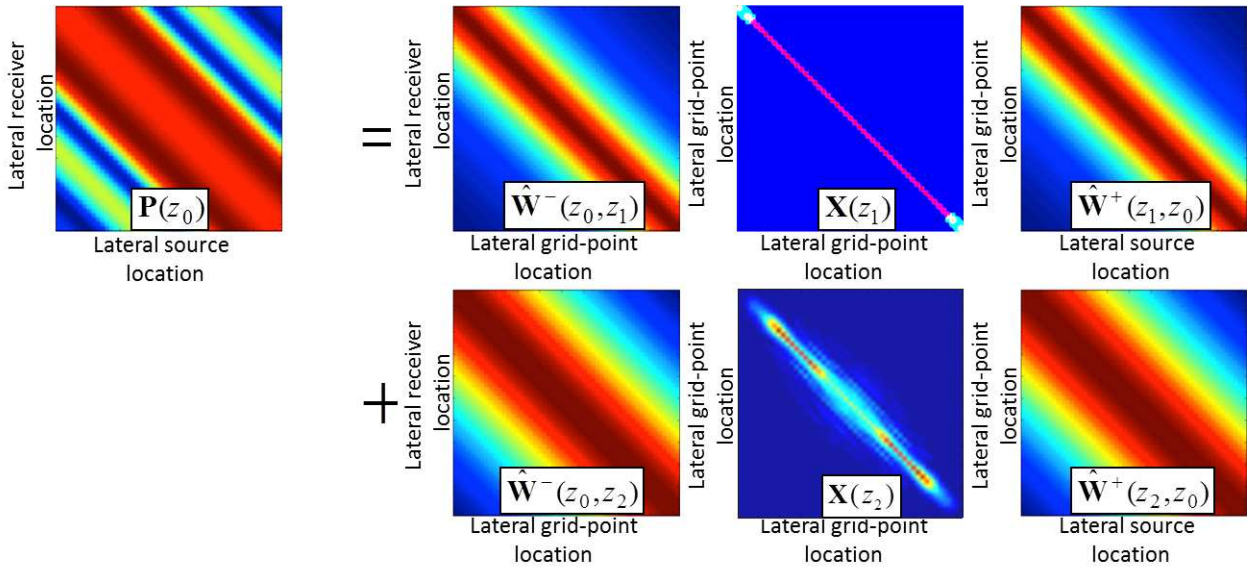

Fig. 3: Graphical representation of equation 9 for the dominant frequency ($15Hz$) from a dataset with three reflection events.

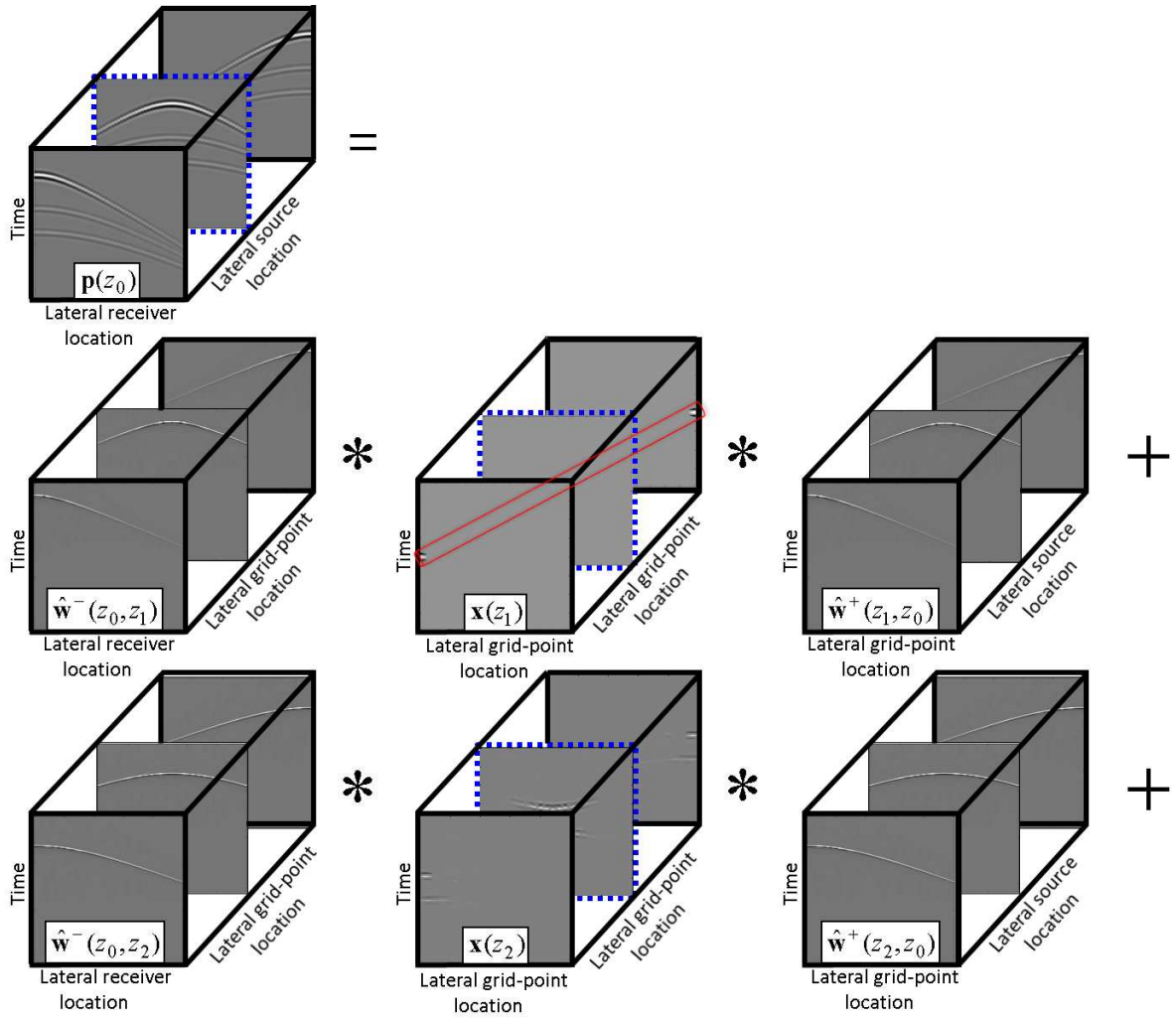

Fig. 4: Graphical representation of the creation of seismic data with the concept of double focal transformation in the space-time domain. The stars denote multi-shift-convolutions. The middle sections of the shot record and the two focal domains (blue edges) are also displayed in Figure 5a-c.

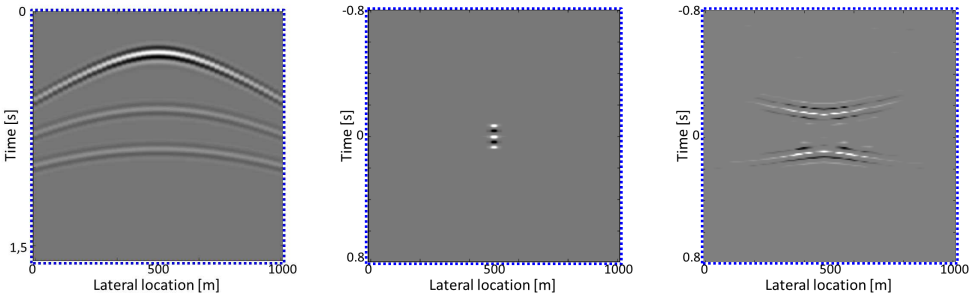

(a) (b) (c)

Fig. 5: (a) Middle shot record of a dataset generated from a subsurface model with three reflectors. In (b) the middle section of the first focal domain is displayed and in (c) the middle section of the second focal domain. All these sections are marked by blue dashed edges in Figure 4. In (b) the first reflector is well focused to a band-limited spike. In (c) the second focal operator is used for the second and third reflector. The result is two compressed events in the second focal domain, which represent reflectivity as well as residual spatial phase.

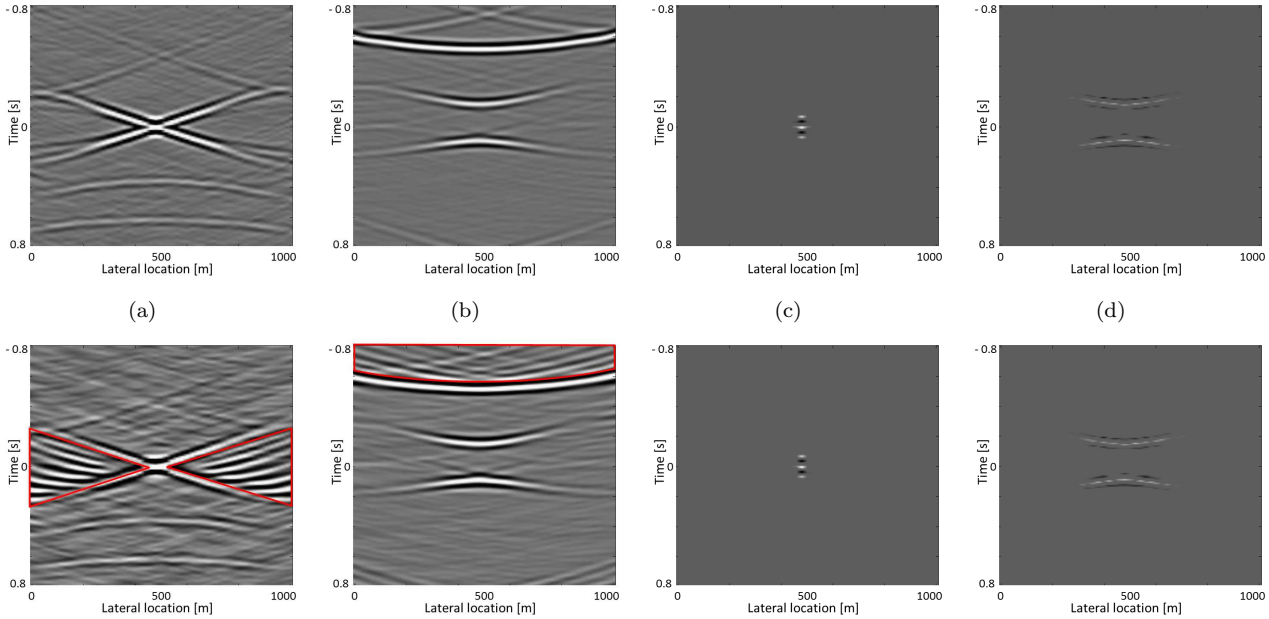

Fig. 6: The middle sections of the first and second focal domain are shown in (a) and (b), which are are derived from dense input data using least-squares inversion. In (e) and (f) coarse input data was used instead. In (c) and (d) the first and second focal domain are derived from the dense input data via sparse inversion and in (g) and (h) coarse input data was used.

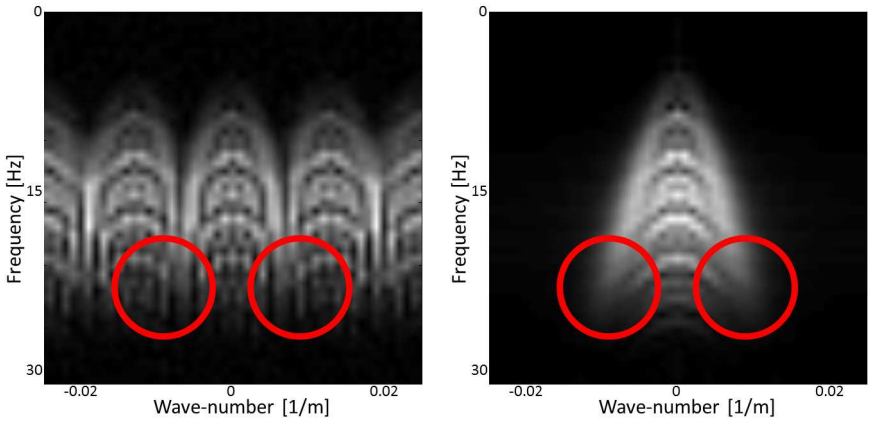

(a) (b)

Fig. 7: (a) The FK plot of the coarse input data. (b) The FK plot of the reconstruction result using sparse inversion. The red circles denote the areas where signal content and aliasing noise overlap for the coarse input data in (a).

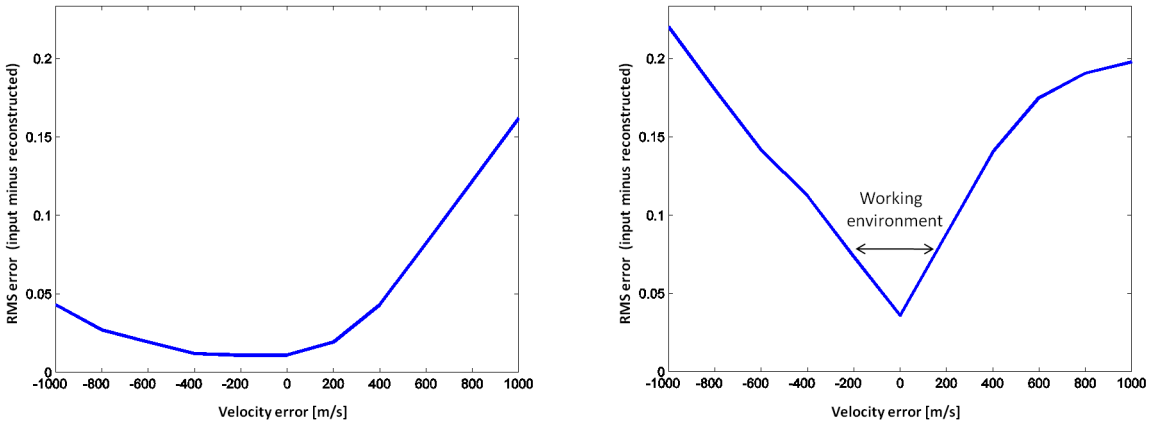

Fig. 8: Plots of the data mismatch as a function of the velocity-error of the focal operator. The horizontal axis depicts the velocity error of the focal operator compared to the true velocity model. The vertical axis denotes the relative data mismatch of the focal-reconstructed data to the input data. In (a) the input data is dense and in (b) the input data is coarse. In both cases the densely sampled traces are taken into account to compute the data-mismatch.

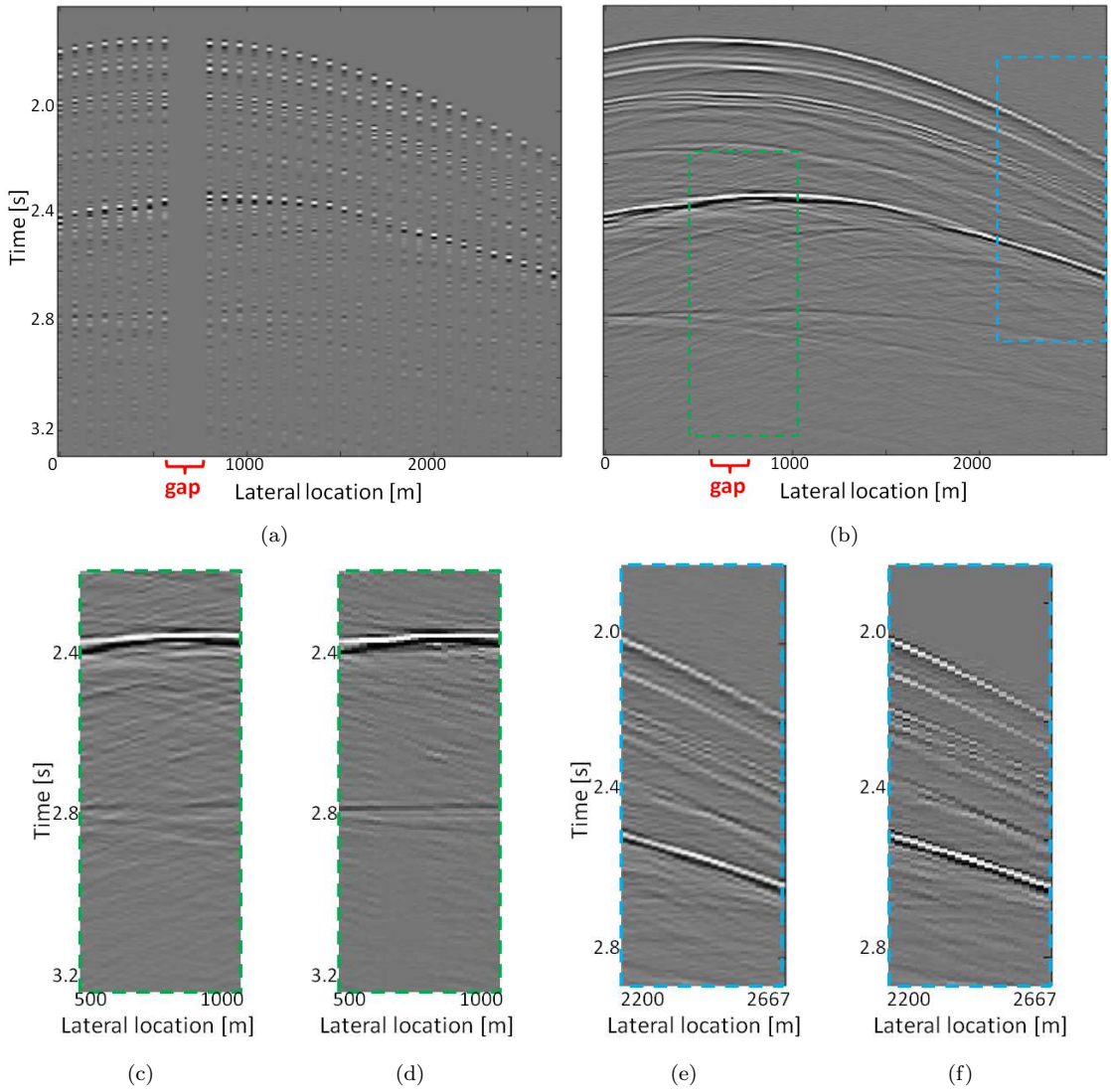

Fig. 9: Field data example. Strongly spatially aliased receiver gather (a) and reconstructed receiver gather using the multi-level focal reconstruction (b). The reconstruction results are displayed zoomed for the near-offset range (c) and the mid/far-offset range (e). The reconstruction results of the multi-gather linear Radon transformation are displayed zoomed for the near-offset range (d) and the mid/far-offset range (f).

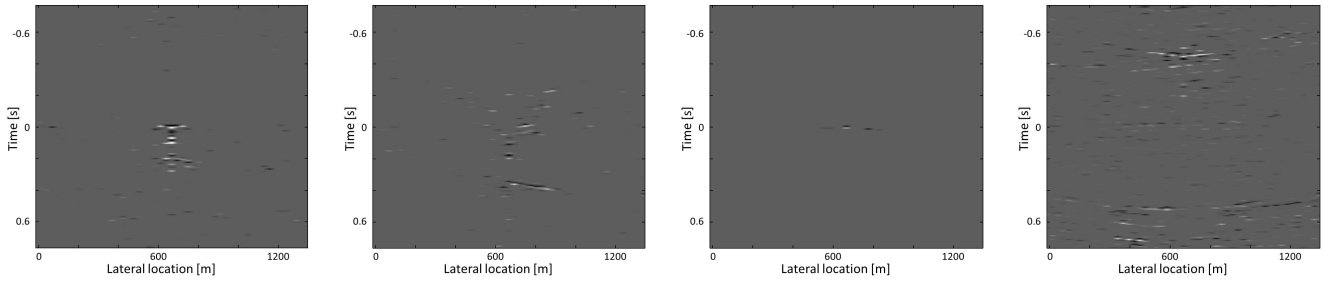

Fig. 10: The middle sections of the four focal domains (a-d) that were obtained from the coarse input data (Figure 9a) by 200 spgl1 iterations solving equation 11.

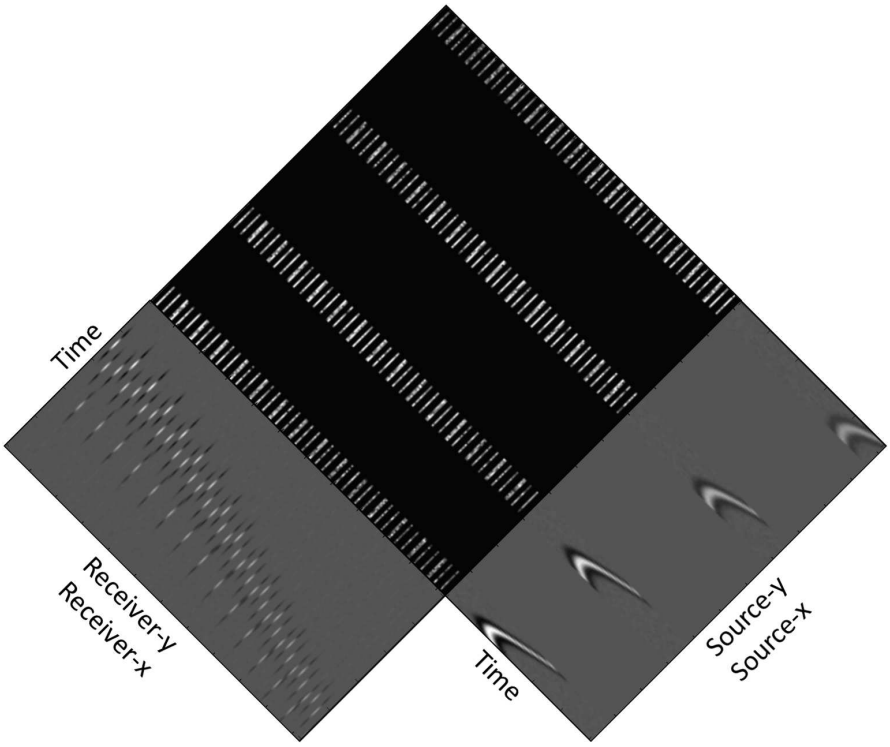

(a)

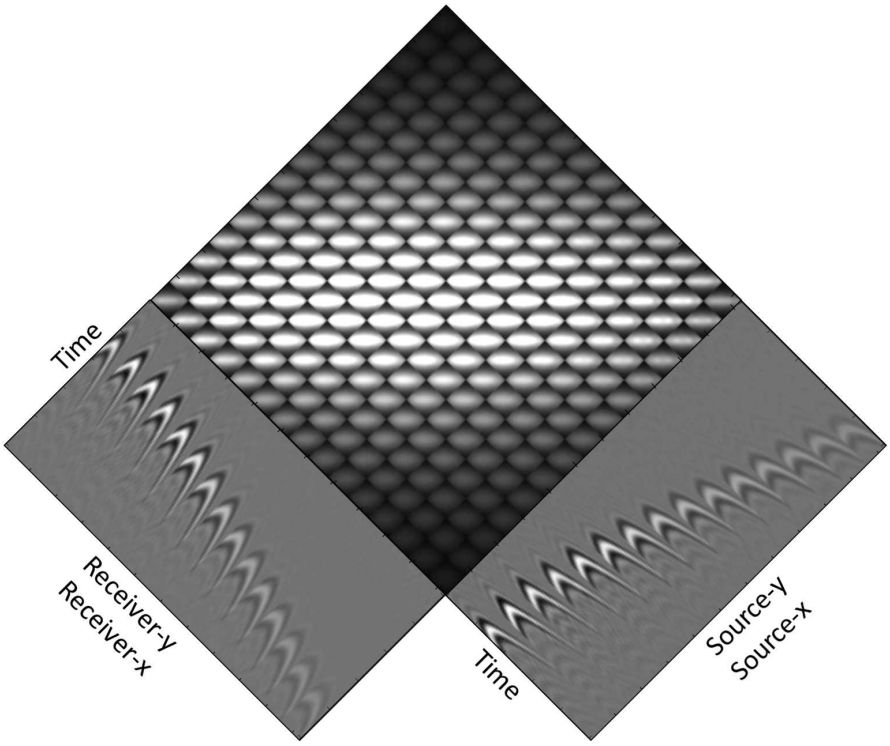

(b)

Fig. 11: The full 3D input dataset is displayed in (a). Viewed from the left hand side receivers are visible that correspond to one example common shot gather. Viewed from the right hand side the sources are visible that correspond to one example common receiver gather. The top view shows a frequency slice to demonstrate the coarse sampling. The receiver-x and source-y sampling is $75m$. The receiver-y and source-x sampling is $15m$. In (b) the receiver-x and source-y sampling is reconstructed to a $15m$ spacing via 3D-double-focal transformation.

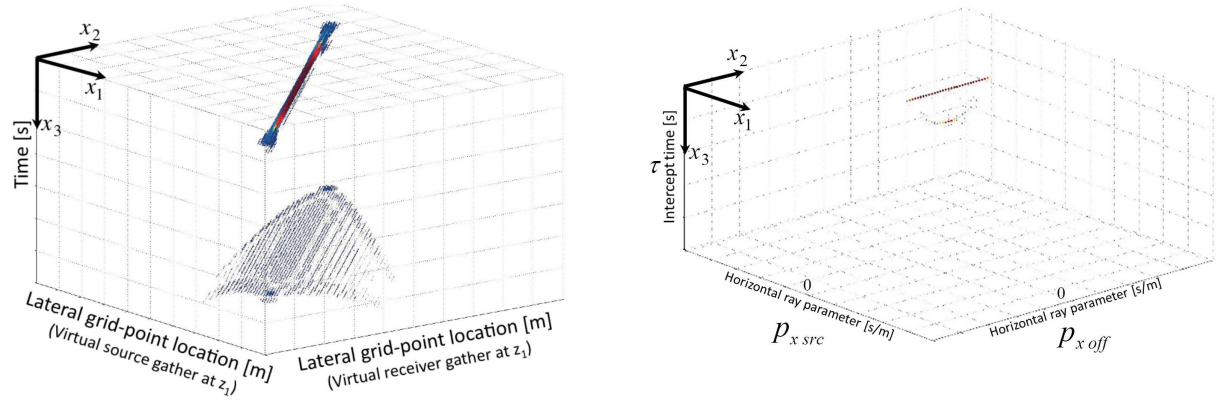

(a) (b)

Fig. 12: (a) The focal domain as a tensor for a 2D fixed spread dataset from a two-reflector subsurface. In (b) the focal domain of (a) is transformed with an additional linear Radon transformation in both lateral directions.

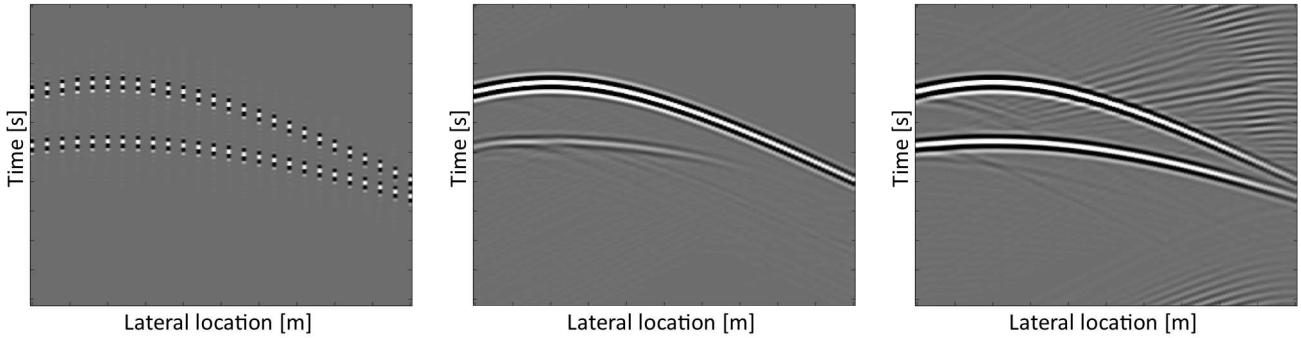

(a) (b) (c)

Fig. 13: A typical coarsely sampled shot record (a), the reconstruction after 10 spgl1 iterations using the double focal transformation (b) and after 10 iterations using the double-focal-double-radon transformation (c).

References

Abramowitz, M., and Stegun, I. A., 1970, Handbook of mathematical function; with formulas, graphs, and mathematical tables: Dover Publications, Inc.

Bagaini, C., and Spagnolini, U., 1996, 2-D continuation operators and their applications: Geophysics, **61**, no. 6, 1846–1858.

Berkhout, A. J., and Verschuur, D. J., 2006, Focal transformation, an imaging concept for signal restoration and noise removal: Geophysics, **71**, no. 6, A55–A59.

Berkhout, A. J., Verschuur, D. J., and Romijn, R., 2004, Reconstruction of seismic data using the focal transformation: 74th Ann. Internat. Mtg., Soc. Expl. Geophys., Expanded abstracts, 1993–1996.

Berkhout, A. J., 1982, Seismic migration, imaging of acoustic energy by wave field extrapolation, A: theoretical aspects: Elsevier (second edition).

Berkhout, A. J., 1987, Applied seismic wave theory: Elsevier.

Berkhout, A. J., 1997, Pushing the limits of seismic imaging, part II: integration of prestack migration, velocity estimation and AVO analysis: Geophysics, **62**, no. 3, 954–969.

Berkhout, A. J., 2006, Seismic processing in the inverse data space: Geophysics, **71**, no. 4, A29–A33.

Biondi, B., Fomel, S., and Chemingui, N., 1998, Azimuth moveout for 3-d prestack imaging: GEOPHYSICS, **63**, no. 2, 574–588.

Cary, P., 1999, Common-offset-vector gathers: An alternative to cross-spreads for wide-azimuth 3-D surveys: Common-offset-vector gathers: An alternative to cross-spreads for wide-azimuth 3-D surveys:, SEG Technical Program Expanded Abstracts 1999, 1496–1499.

de Bruin, C. G. M., Wapenaar, C. P. A., and Berkhout, A. J., 1990, Angle-dependent reflectivity by means of prestack migration: Geophysics, **55**, no. 9, 1223–1234.

Deregowski, S. M., 1986, What is DMO?:, *in* First Break 1986, 4, 7–24.

Doulgeris, P., Mahdad, A., and Blacquiere, G., 2009, An R-based overview of the WRW concept: 3rd International Conference and Exhibition, Nafplion, Greece, 21-26 June, 2009.

Doulgeris, P., Verschuur, D. J., and Blacquiere, G., 2012, Separation of blended data by sparse inversion utilizing surface-related multiples: 74rd Ann. Internat. Mtg., Eur. Ass. of Expl. Geophys., Expanded abstracts, A041.

Dragoset, W. H., 1999, A practical approach to surface multiple attenuation: The Leading Edge, **18**, no. 1, 104–108.

Duijndam, A., Schonewille, M., and Hindriks, C., 1999, Reconstruction of band- limited signals, irregularly sampled along one spatial direction: Geophysics, **64**, no. 2, 524–538.

Fokkema, J. T. ., and van den Berg, P. M., 1993, Seismic applications of acoustic reciprocity: Elsevier Science Publishers B.V.

Gisolf, A., and Verschuur, D. J., 2010, The principles of quantitative acoustical imaging: EAGE publications bv.

Hennenfent, G., and Herrmann, F. J., 2008, Simply denoise: Wavefield reconstruction via jittered undersampling: Geophysics, **73**, no. 3, V19–V28.

Hennenfent, G., Fenelon, L., and Herrmann, F. J., 2010, Nonequispaced curvelet transform for seismic data reconstruction: A sparsity-promoting approach: Geophysics, **75**, no. 6, WB203–WB210.

Herrmann, P., Mojesky, T., Magasan, M., and Hugonnet, P., 2000, De-aliased, high-resolution Radon transforms: 70th Ann. Internat. Mtg., Soc. Expl. Geophys., Expanded abstracts, 1953–1956.

Kabir, M. M. N., and Verschuur, D. J., 1995, Restoration of missing offsets by parabolic radon transform: Geophys. Prosp., **43**, no. 3, 347–368.

Kinneging, N. K., Budejicky, V., Wapenaar, C. P. A., and Berkhout, A. J., 1989, Efficient 2D and 3D shot record redatuming: Geophys. Prosp., **37**, no. 5, 493–530.

Kontakis, A., and Verschuur, D. J., 2014, Deblending via sparsity-constrained inversion in the focal domain: 76th Ann. Internat. Mtg., Eur. Ass. of Geosc. and Eng., Expanded abstracts, Th ELI2 02.

Kontakis, A., and Verschuur, D. J., 2015, Deblending via a hybrid focal and linear Radon transform: 77th EAGE Conference and Exhibition, EAGE, Extended Abstracts, We N101 02.

Kuehl, H., 2002, Least-squares wave-equation migration/inversion: Ph.D. thesis, University of Alberta (Canada).

Kutscha, H., and Verschuur, E., 2012, Data reconstruction via sparse double focal transformation: An overview.: IEEE Signal Process. Mag., **29**, no. 4, 53–60.

Kutscha, H., Verschuur, D., and Berkhout, A., 2010, High resolution double focal transformation and its application to data reconstruction:, *in* SEG Technical Program Expanded Abstracts 2010, 3589–3593.

Kutscha, H., 2014, The double focal transformation and its application to data reconstruction: Ph.D. thesis, Delft University of Technology (Netherlands).

Lopez, G. A., and Verschuur, D. J., 2013, 3D primary estimation by sparse inversion using the focal domain parameterization: 83th Ann. Internat. Mtg., Soc. Expl. Geophys., Expanded abstracts, 4172–4175.

Naghizadeh, M., and Sacchi, M. D., 2010, Beyond alias hierarchical scale curvelet interpolation of regularly and irregularly sampled seismic data: Geophysics, **75**, no. 6, WB189–WB202.

Naghizadeh, M., 2012, Seismic data interpolation and denoising in the frequency-wavenumber domain: Geophysics, **77**, no. 2, V71–V80.

Nemeth, T., Wu, C., and Schuster, G., 1999, Least squares migration of incomplete reflection data: Geophysics, **64**, no. 1, 208–221.

Schonewille, M., Klaedtke, A., and Vigner, A., 2009, Anti alias anti leakage Fourier transform:, *in* SEG Technical Program Expanded Abstracts 2009, 3249–3253.

Spagnolini, U., and Opreni, S., 1996, 3D shot continuation operator:, *in* SEG Technical Program Expanded Abstracts 1996, 439–442.

Trad, D. O., Ulrych, T., and Sacchi, M., 2003, Latest views of the sparse radon transform: Geophysics, **68**, 386–399.

Trad, D. O., 2002, Accurate interpolation with high-resolution time-variant radon transforms: Geophysics, **67**, no. 2, 644–656.

Trad, D. O., 2003, Interpolation and multiple attenuation with migration operators: Geophysics, **68**, 2043–2054.

Trad, D. O., 2009, Five-dimensional interpolation: Recovering from acquisition constraints: Geophysics, **74**, no. 6, V123–V132.

van den Berg, E., and Friedlander, M. P., 2008, Probing the pareto frontier for basis pursuit solutions: SIAM J. Sci. Comput., **31**, no. 2, 890–912.

van Wijngaarden, A. J., 1998, Imaging and characterization of angle-dependent seismic reflection data: Ph.D. thesis, Delft University of Technology.

Verschuur, D. J., Vrolijk, J. W., and Tsingas, C., 2012, 4d reconstruction of wide azimuth (waz) data using sparse inversion of hybrid radon transforms:, *in* SEG Technical Program Expanded Abstracts 2012, 1–5.

Wang, J., Ng, M., and Perz, M., 2010, Seismic data interpolation by greedy local radon transform: Geophysics, **75**, no. 6, WB225–WB234.

Xu, S., Zhang, Y., Pham, D., and Lambare, G., 2005, Antileakage fourier transform for seismic data regularization: Geophysics, **70**, no. 4, V87–V95.

Zwartjes, P. M., and Gisolf, A., 2006, Fourier reconstruction of marine-streamer data in four spatial coordinates: Geophysics, **71**, no. 6, V171–V186.

Zwartjes, P. M., and Gisolf, A., 2007, Fourier reconstruction with sparse inversion: Geophys. Prosp., **55**, no. 2, 199–221.

Zwartjes, P., and Sacchi, M., 2007, Fourier reconstruction of nonuniformly sampled, aliased seismic data: Geophysics, **72**, no. 1, V21–V32.